Acta Crystallographica Section D
Biological Crystallography
ISSN 1399-0047

Structure-based characterization and antifreeze properties of a hyperactive ice-binding protein from the Antarctic bacterium *Flavobacterium frigoris* PS1

Hackwon Do,[a,b] Soon-Jong Kim,[c] Hak Jun Kim[d] and Jun Hyuck Lee[a,b]*

[a]Division of Polar Life Sciences, Korea Polar Research Institute, Incheon 406-840, Republic of Korea, [b]Department of Polar Sciences, University of Science and Technology, Incheon 406-840, Republic of Korea, [c]Department of Chemistry, Mokpo National University, Chonnam 534-729, Republic of Korea, and [d]Department of Chemistry, Pukyong National University, Busan 608-739, Republic of Korea

Correspondence e-mail: junhyucklee@kopri.re.kr

Received 11 December 2013
Accepted 15 January 2014

PDB references: FfIBP, 4nu2; mFfIBP, 4nu3; mLeIBP, 4nuh

Ice-binding proteins (IBPs) inhibit ice growth through direct interaction with ice crystals to permit the survival of polar organisms in extremely cold environments. FfIBP is an ice-binding protein encoded by the Antarctic bacterium *Flavobacterium frigoris* PS1. The X-ray crystal structure of FfIBP was determined to 2.1 Å resolution to gain insight into its ice-binding mechanism. The refined structure of FfIBP shows an intramolecular disulfide bond, and analytical ultracentrifugation and analytical size-exclusion chromatography show that it behaves as a monomer in solution. Sequence alignments and structural comparisons of IBPs allowed two groups of IBPs to be defined, depending on sequence differences between the α2 and α4 loop regions and the presence of the disulfide bond. Although FfIBP closely resembles *Leucosporidium* (recently re-classified as *Glaciozyma*) IBP (LeIBP) in its amino-acid sequence, the thermal hysteresis (TH) activity of FfIBP appears to be tenfold higher than that of LeIBP. A comparison of the FfIBP and LeIBP structures reveals that FfIBP has different ice-binding residues as well as a greater surface area in the ice-binding site. Notably, the ice-binding site of FfIBP is composed of a T-A/G-*X*-T/N motif, which is similar to the ice-binding residues of hyperactive antifreeze proteins. Thus, it is proposed that the difference in TH activity between FfIBP and LeIBP may arise from the amino-acid composition of the ice-binding site, which correlates with differences in affinity and surface complementarity to the ice crystal. In conclusion, this study provides a molecular basis for understanding the antifreeze mechanism of FfIBP and provides new insights into the reasons for the higher TH activity of FfIBP compared with LeIBP.

1. Introduction

Ice-binding proteins (IBPs) produced by polar organisms inhibit the growth of ice crystals to protect themselves from freezing damage. These proteins include antifreeze proteins (AFPs), ice-recrystallization inhibition proteins and ice-nucleation proteins (D'Amico *et al.*, 2006; Davies *et al.*, 2002; Venketesh & Dayananda, 2008; Jia & Davies, 2002). IBPs have the property of binding to ice crystals, thereby inhibiting the growth of extracellular ice crystals and protecting the organism against osmotic shock and physical damage. A wide range of both structures and ice-binding mechanisms have been discovered in the study of IBPs. To date, nuclear magnetic resonance (NMR) and crystal structures of AFPs from polar fish (Kwan *et al.*, 2005; Patel & Graether, 2010; Marshall *et al.*, 2005; Liu *et al.*, 2007; Achenbach & Ewart, 2002; Antson *et al.*, 2001; Siemer & McDermott, 2008), insects

(Graether *et al.*, 2000; Hakim *et al.*, 2013; Doucet *et al.*, 2000; Graether & Sykes, 2004; Liou *et al.*, 2000), plants (Middleton *et al.*, 2012; Smallwood *et al.*, 1999) and psychrophilic bacteria (Raymond *et al.*, 2008; Garnham *et al.*, 2008, 2011) have been reported. The structures of insect and bacterial AFPs exhibit a β-helical fold, and these proteins have a regular pattern of ice-binding residues. Two Thr residues are aligned in insect AFPs (Thr-*X*-Thr motif), which may allow the protein to bind to two different basal and prism planes of ice (Leinala, Davies & Jia, 2002). In contrast, the bacterial MpAFP uses a Thr-*X*-Asx motif located in a flat β-sheet to bind ice (Garnham *et al.*, 2008). Mutational studies have shown that substitution of the Thr residue with Tyr results in a loss of antifreeze activity (Garnham *et al.*, 2008; Venketesh & Dayananda, 2008; Lee *et al.*, 2012). These data suggest that the Thr residues located in the ice-binding face are involved in ice binding. The β-helical fold provides a conserved ice-binding platform, forming a flat binding surface and a common Thr-containing motif. It has commonly been thought that the ice-binding sites are relatively flat in order to provide good surface–surface complementarity to the ice crystal (Leinala, Davies & Jia, 2002; Graether *et al.*, 2000).

Recently, new ice-binding proteins (IBPs) have been identified in Antarctic sea-ice algae (Raymond *et al.*, 2009; Bayer-Giraldi *et al.*, 2011; Janech *et al.*, 2006; Krell *et al.*, 2008), fungi (Hoshino *et al.*, 2003; Xiao *et al.*, 2010; Kondo *et al.*, 2012), mushrooms (Raymond & Janech, 2009), bacteria (Do *et al.*, 2012; Raymond *et al.*, 2007) and the Arctic yeast *Leucosporidium* sp. AY30 (Lee *et al.*, 2010, 2012; Park *et al.*, 2011, 2012). The IBPs have low sequence similarity to other known AFPs and adopt a unique ice-binding mechanism. Recently, the crystal structure of IBP from *Leucosporidium* sp. AY30 (LeIBP) was determined in our laboratory (Lee *et al.*, 2012). Structural and functional studies of LeIBP have shown that it has a β-helical fold similar to those of insect and bacterial AFPs (Lee *et al.*, 2012). However, LeIBP shows a number of characteristics that are distinct from insect and bacterial AFPs, thereby suggesting that it can be classified into a new IBP family. In addition, the ice-binding site of LeIBP is complex and does not have a simple ice-binding motif. In contrast, insect and bacterial AFPs use the Thr-*X*-Thr and Thr-*X*-Asx motifs, respectively, located in a flat β-sheet to bind ice.

Another IBP (FfIBP) from the Antarctic bacterium *Flavobacterium frigoris* PS1 has recently been identified

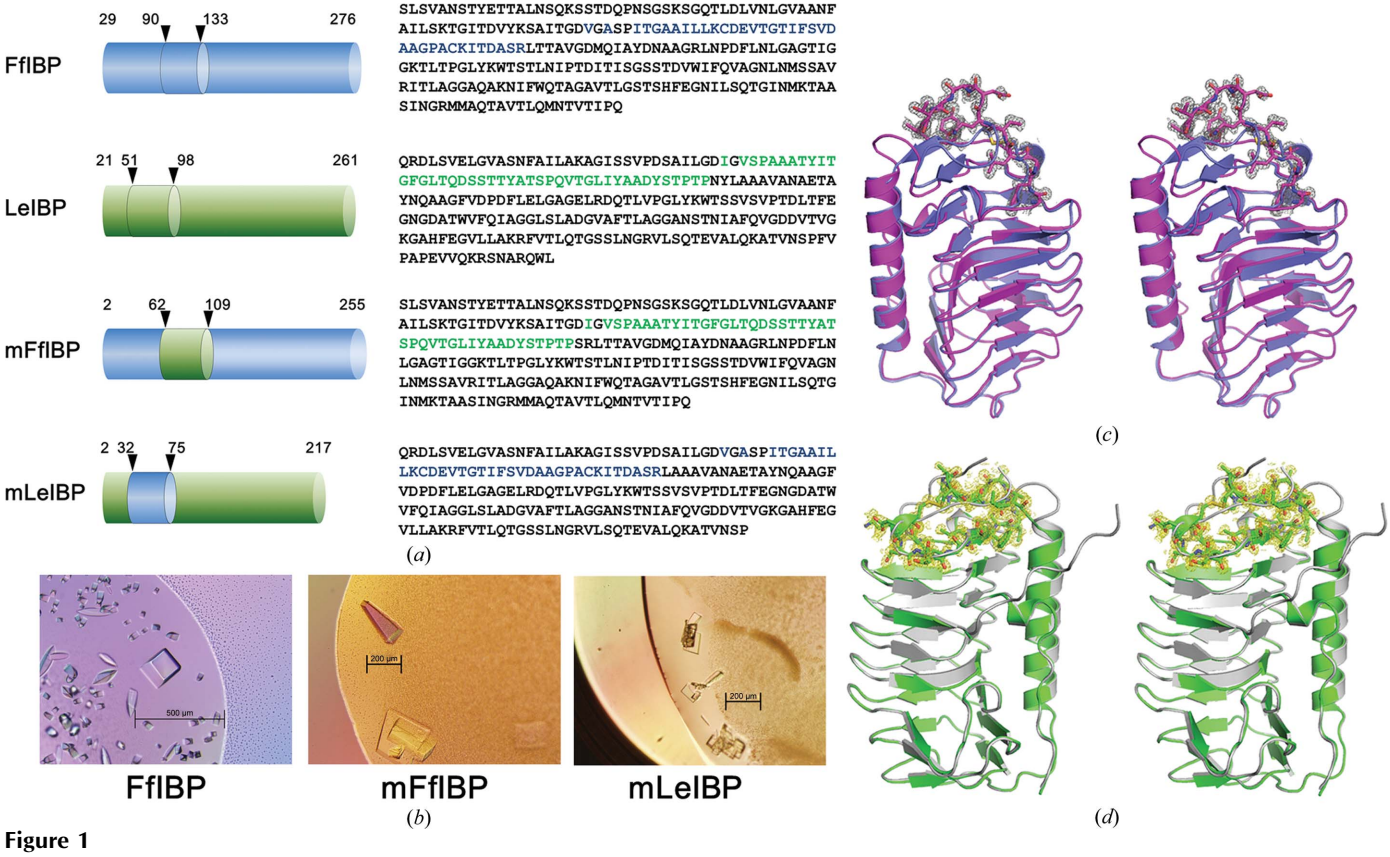

Figure 1
Capping loop structure of mFfIBP and mLeIBP. (*a*) Schematic diagram and amino-acid sequences of FfIBP, LeIBP, mFfIBP and mLeIBP. Two chimeric proteins (mFfIBP and mLeIBP) were constructed in which the α4–β5 connecting loop sequences (blue or green) were swapped. (*b*) Crystal images of FfIBP (left panel; the scale bar is 500 µm in length), mFfIBP (middle panel; the scale bar is 200 µm in length) and mLeIBP (right panel; the scale bar is 200 µm in length). (*c*) Stereoview of the superimposed crystal structures of wild-type FfIBP (slate blue) and chimeric mFfIBP (magenta). A $2F_o - F_c$ electron-density map (contoured at 1σ) is shown in the area of the capping loop region (resides 78–89) in the mFfIBP structure. (*d*) Stereoview of the structural superposition of mLeIBP (green) on LeIBP (grey). A $2F_o - F_c$ electron-density map (contoured at 1σ) is shown in the area of the capping loop region (resides 47–69) in the mLeIBP structure. For an improved view and a comparison of the cap region structure, the mLeIBP structure in (*d*) was rotated by 180° compared with the orientation of the mFfIBP structure.

(GenBank accession No. AHKF00000000.1; Raymond & Kim, 2012) and characterized (Do *et al.*, 2012). FfIBP shows 56% sequence similarity to LeIBP, but it has an up to tenfold higher antifreeze activity than LeIBP. In this study, we describe the crystal structure of FfIBP and compare this structure with other known structures in order to understand their ice-binding modes. Indeed, FfIBP functions as a monomer and has a unique ice-binding site containing a T-A/G-*X*-T/N motif. Conclusively, our studies suggest that free accessibility as a monomer, and more regularly aligned ice-binding residues, may confer higher thermal hysteresis (TH) activity on FfIBP.

2. Materials and methods

2.1. Expression and purification of IBPs

Recombinant FfIBP was expressed, purified and crystallized as described previously (Do *et al.*, 2012). Briefly, the region of the FfIBP gene encoding amino-acid residues 29–276 was amplified by PCR, and the *Nde*I–*Xho*I-digested fragment was then subcloned into the pCold I expression vector (Takara Bio Inc., Shiga, Japan). The resulting expression constructs contained an N-terminal 6×His-tag fusion protein with a factor Xa protease site for cleaving the tag. The cloned nucleotide sequence was confirmed by DNA sequencing (Genotech Co., Republic of Korea) and the expression construct was transformed into *Escherichia coli* strain BL21 (DE3) (Invitrogen, Carlsbad, California, USA). The cells were grown at 37°C in LB medium containing 100 mg l^{-1} ampicillin and induced at an OD_{600} of 0.6 by adding a 1 m*M* final concentration of IPTG. The cells were cultivated for an additional 18 h at 16°C and harvested by centrifugation at 8000*g* for 15 min. The bacterial pellet was lysed by sonication in sonication buffer (50 m*M* Na_2HPO_4 pH 8.5, 300 m*M* NaCl, 5 m*M* imidazole). The lysate was clarified by centrifugation (16 000 rev min^{-1} for 1 h at 4°C) and loaded onto an Ni–NTA agarose column pre-equilibrated with lysis buffer (50 m*M* Na_2HPO_4 pH 8.5, 300 m*M* NaCl, 5 m*M* imidazole). The bound protein was eluted with a 400 m*M* imidazole gradient. The fractions containing FfIBP were pooled and factor Xa protease was added at a 1:50 molar ratio (to cleave the 6×His tag). After cleavage of the 6×His tag at 4°C overnight, the FfIBP was further purified using a Superdex 200 size-exclusion column (SEC; Amersham Pharmacia) equilibrated in SEC loading buffer (20 m*M* Tris–HCl pH 8.5, 150 m*M* NaCl). The fractions containing FfIBP were pooled and concentrated to 16.4 mg ml^{-1}.

The nucleotides encoding mFfIBP and mLeIBP (two novel chimeric proteins generated by swapped the capping head regions) were chemically synthesized by Bioneer Co. (Daejeon, Republic of Korea) and the precise sequences are shown in Fig. 1. The synthesized mutant genes were subcloned into pET-28a(+) vector (Novagen, Madison, Wisconsin, USA) between the *Nde*I and *Xho*I restriction-enzyme sites and were expressed in *E. coli* strain BL21 (DE3). The subsequent protein-expression and purification steps of mFfIBP and mLeIBP were similar to those used for wild-type FfIBP, except for the growth temperature and thrombin treatment. Briefly, the growth and induction of the mutant-expressing cells were consistently performed at 20°C and thrombin digestion (0.2 U thrombin per milligram of mutant protein) was performed to remove the N-terminal hexahistidine tag at 4°C overnight prior to the SEC experiment.

2.2. Crystallization of IBPs

Initial crystallization conditions were obtained and preliminary X-ray diffraction data analysis was performed as reported previously (Do *et al.*, 2012). In this study, the resolution of the FfIBP structure was extended to 2.1 Å under identical crystallization conditions and in the same space group ($P4_122$). The best-diffracting crystals of FfIBP were grown using hanging-drop vapour diffusion at 20°C and were obtained by mixing 1.0 µl protein solution (16.4 mg ml^{-1}) with 1.0 µl crystallization solution (0.1 *M* sodium acetate pH 4.4, 3 *M* sodium chloride). Large single crystals grew to maximum dimensions of 0.2 mm in all directions within 2–3 d (Fig. 1*b*). Crystals were cooled for X-ray diffraction using Paratone as a cryoprotectant.

For crystallization of mFfIBP, the purified protein was concentrated to approximately 23.1 mg ml^{-1} using Amicon Ultra-15 centrifugal ultrafiltration (Millipore, Bedford, Massachusetts, USA). Initial crystal screening was performed with commercially available screening kits such as MCSG-1–4 (Microlytic, Burlington, Massachusetts, USA), Wizard Classics 1–4 (Emerald Bio, Seattle, Oregon, USA) and The Classics and Classics II Suites (Qiagen, Hilden, Germany) using the sitting-drop method by mixing 0.8 µl protein solution with 0.8 µl reservoir solution at 293 K. Initial microcrystals were obtained from The Classics Suite condition No. 58 (0.1 *M* Tris–HCl pH 8.5, 1.0 *M* lithium sulfate, 0.01 *M* nickel chloride), The Classics Suite condition No. 91 [0.2 *M* ammonium sulfate, 30%(*w*/*v*) PEG 4000] and Wizard Classic 1 condition No. 17 [0.1 *M* sodium acetate/acetic acid pH 4.5, 30%(*w*/*v*) PEG 8000, 0.2 *M* lithium sulfate]. These conditions were optimized using variation of the type of precipitant and the pH. In addition, the volume of the drop was increased from 0.8 to 1 µl to generate larger crystals. From these results, the best single crystals of mFfIBP were generated in 2 d with 28–30.5%(*w*/*v*) PEG 4000, 0.19 *M* ammonium sulfate at 293 K using the hanging-drop vapour-diffusion method in 24-well plates (Fig. 1*b*).

Crystallization screening trials of mLeIBP were set up in 96-well plates with the commercial screening kits MCSG-1–4 (Microlytic), Wizard Classics 1–4 (Emerald Bio) and The Classics and Classics II Suites (Qiagen). Initial microcrystals were obtained from MCSG-1 condition No. 21 [25%(*w*/*v*) PEG 3350, 0.2 *M* magnesium chloride], MCSG-1 condition No. 23 [0.1 *M* Tris–HCl pH 8.5, 20%(*w*/*v*) PEG 8000, 0.2 *M* magnesium chloride], MCSG-4 condition No. 72 [0.1 *M* Tris–HCl pH 8.5, 30%(*w*/*v*) PEG 4000, 0.2 *M* magnesium chloride], The Classics II Suite condition No. 84 [0.1 *M* HEPES pH 7.5, 25%(*w*/*v*) PEG 3350, 0.2 *M* magnesium chloride] and The Classics II Suite condition No. 85 [0.1 *M* Tris–HCl pH 8.5, 25%(*w*/*v*) PEG 3350, 0.2 *M* magnesium chloride].

Table 1
Data-collection and refinement statistics.

Values in parentheses are for the highest resolution shell.

Data set	FfIBP	mFfIBP	mLeIBP
X-ray source	Beamline 5C, PAL	Beamline 7A, PAL	Beamline 5C, PAL
Space group	$P4_122$	$P1$	$P1$
Wavelength (Å)	0.9795	0.9793	0.9795
Resolution (Å)	50.00–2.10 (2.14–2.10)	50.00–1.40 (1.42–1.40)	50.00–1.34 (1.36–1.34)
Total reflections	126336	251773	106736
Unique reflections	25914 (1250)	82929 (3354)	30805 (1569)
Average $I/\sigma(I)$	47.1 (11.9)	29.0 (9.0)	48.0 (25.5)
R_{merge}†	0.062 (0.241)	0.061 (0.175)	0.047 (0.092)
Multiplicity	4.9 (4.8)	3.0 (2.9)	3.5 (3.4)
Completeness (%)	98.2 (99.1)	93.3 (75.0)	90.5 (93.3)
Refinement			
Resolution (Å)	37.81–2.10 (2.15–2.10)	25.19–1.40 (1.41–1.40)	44.16–1.34 (1.38–1.34)
No. of reflections in working set	24498 (1760)	78787 (4924)	29246 (2151)
No. of reflections in test set	1309 (80)	4133 (255)	1559 (108)
No. of amino-acid residues	216	452	216
No. of water molecules	57	836	307
R_{cryst}‡	0.207 (0.277)	0.219 (0.240)	0.166 (0.253)
R_{free}§	0.241 (0.316)	0.234 (0.289)	0.201 (0.259)
R.m.s.d., bond lengths (Å)	0.023	0.014	0.021
R.m.s.d., bond angles (°)	2.185	1.576	2.077
Average B value (Å^2)			
Protein	39.85	8.84	12.12
Solvent	45.18	23.01	25.09

† $R_{merge} = \sum_{hkl}\sum_i |I_i(hkl) - \langle I(hkl)\rangle|/\sum_{hkl}\sum_i I_i(hkl)$. ‡ $R_{cryst} = \sum_{hkl}||F_{obs}| - |F_{calc}||/\sum_{hkl}|F_{obs}|$. § R_{free} was calculated with 5% of all reflections excluded from the refinement stages using high-resolution data.

Optimization screens were performed in 24-well plates using the hanging-drop vapour-diffusion technique with 1 µl well solution mixed with 1 µl protein solution (at 17.4 mg ml^{-1}) and the drops were equilibrated against 0.5 ml of the same precipitant solution. The best single crystals of mLeIBP were grown at 20°C in an optimal crystallization solution [0.1 *M* Tris–HCl pH 8.9, 0.2 *M* magnesium chloride, 34%(*w*/*v*) PEG 4000]. Plate-shaped crystals of about 0.1 × 0.15 × 0.15 mm in size grew in 3 d at 20°C (Fig. 1*b*).

2.3. Data collection and structure determination of IBPs

A native data set for FfIBP was collected to 2.1 Å resolution on beamline 5C at Pohang Accelerator Laboratory (PAL; Pohang, Republic of Korea) and the diffraction images were processed and scaled with *HKL*-2000 (Otwinowski & Minor, 1997). The FfIBP structure was determined by molecular replacement using *MOLREP* (Vagin & Teplyakov, 2010). Molecular replacement is a widely used method to obtain phase information for an unknown structure from previously solved homologous protein structures (Drenth, 1999). The monomer structure of LeIBP (PDB entry 3uyu; Lee *et al.*, 2012) was used as the search model. Refinement of coordinates was performed using iterative rounds of *REFMAC*5 refinement (Murshudov *et al.*, 2011) and manual rebuilding using *Coot* (Emsley *et al.*, 2010). The final model contains residues 61–276 and 57 water molecules in the asymmetric unit, with 97.8% of the residues being located in the most favoured regions of the Ramachandran plot and no residues in the disallowed region, as defined by *MolProbity* (Chen *et al.*, 2010). The model has root-mean-square deviation (r.m.s.d.) values of 0.023 Å for bond lengths and 2.185 Å for bond angles. The R_{cryst} and R_{free} values of the final model are 20.7 and 24.12%, respectively (Table 1).

A complete data set for mFfIBP was collected to 1.4 Å resolution on beamline 7A at PAL. The data were processed with the *HKL*-2000 suite of programs (Otwinowski & Minor, 1997). The mFfIBP crystal belonged to space group $P1$ and had unit-cell parameters a = 31.7, b = 51.5, c = 75.2 Å, α = 104.4, β = 96.9, γ = 97.7°. There were two molecules in the asymmetric unit, giving a solvent content of 44.3% (V_M = 2.21 Å^3 Da^{-1}; Table 1). The initial model structure was solved by molecular replacement with *MOLREP* (Vagin & Teplyakov, 2010) using the refined wild-type FfIBP structure as a search model. The model was then subjected to iterative rounds of refinement using *REFMAC*5 (Murshudov *et al.*, 2011) and *PHENIX* (Adams *et al.*, 2010), followed by manual model building using *Coot* (Emsley *et al.*, 2010). The refined model has a crystallographic R factor of 21.2% and a free R factor of 23.4%. The quality of the final model was checked using *MolProbity* (Chen *et al.*, 2010) and a Ramachandran plot, which showed a *MolProbity* score of 1.80 (54th percentile) and an overall clashscore of 11.1 (43rd percentile), with all residues lying in the favourable region of the Ramachandran plot. The crystallographic data are listed in Table 1.

Diffraction data for mLeIBP were collected on beamline 5C of PAL to 1.34 Å resolution and were processed using *HKL*-2000. The crystal belonged to the triclinic space group $P1$, with unit-cell parameters a = 29.4, b = 31.2, c = 47.1 Å, α = 76.3, β = 72.6, γ = 76.6°. The initial structure of mLeIBP was solved by molecular replacement with *Phaser* (McCoy *et al.*, 2007) using the wild-type FfIBP structure. Iterative cycles of model building were carried out in *Coot* (Emsley *et al.*, 2010) and refinement was performed in *REFMAC* (Murshudov *et al.*, 2011). The mLeIBP crystal contains one protein molecule in the asymmetric unit. Its final refined structure includes residues 2–217 and 307 water molecules. Data-collection and refinement statistics are provided in Table 1.

2.4. Thermal hysteresis activity

The thermal hysteresis (TH) activity of the IBPs was measured as described previously. Briefly, the sample was placed on the stage and cooled rapidly to approximately −20°C using a nanolitre osmometer (Otago Osmometers, Dunedin, New Zealand). Measurements for the TH activity curve were performed in 20 m*M* Tris–HCl pH 8.5, 150 m*M* NaCl buffer and the protein sample concentration ranged

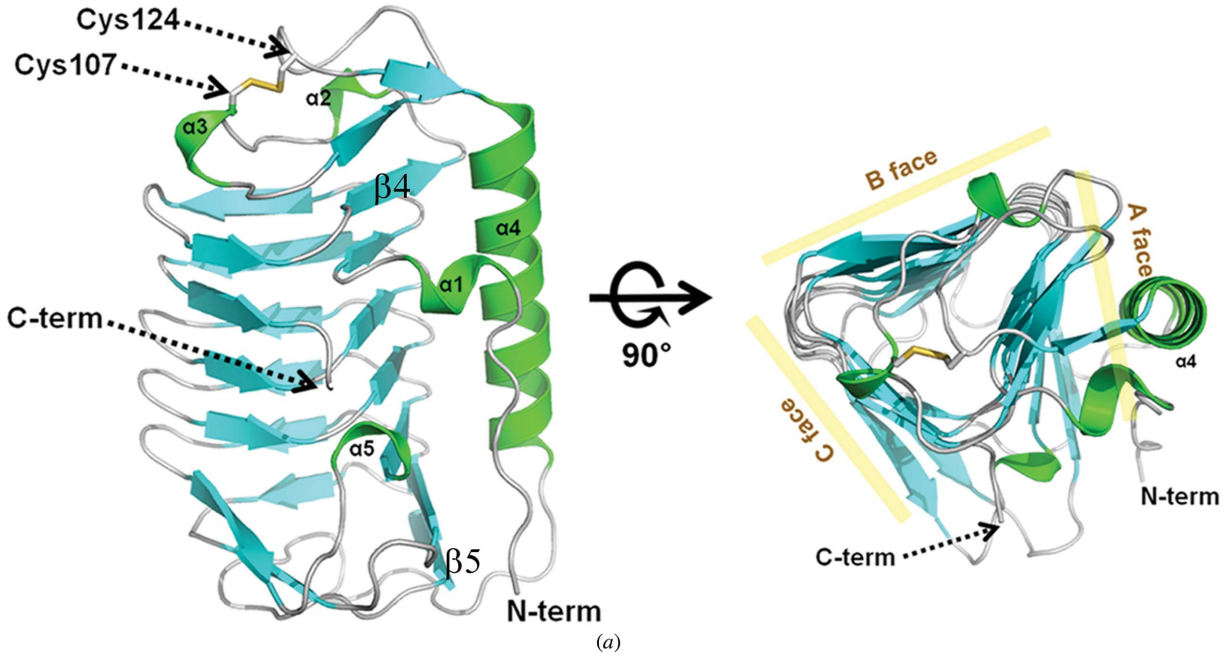

(*a*)

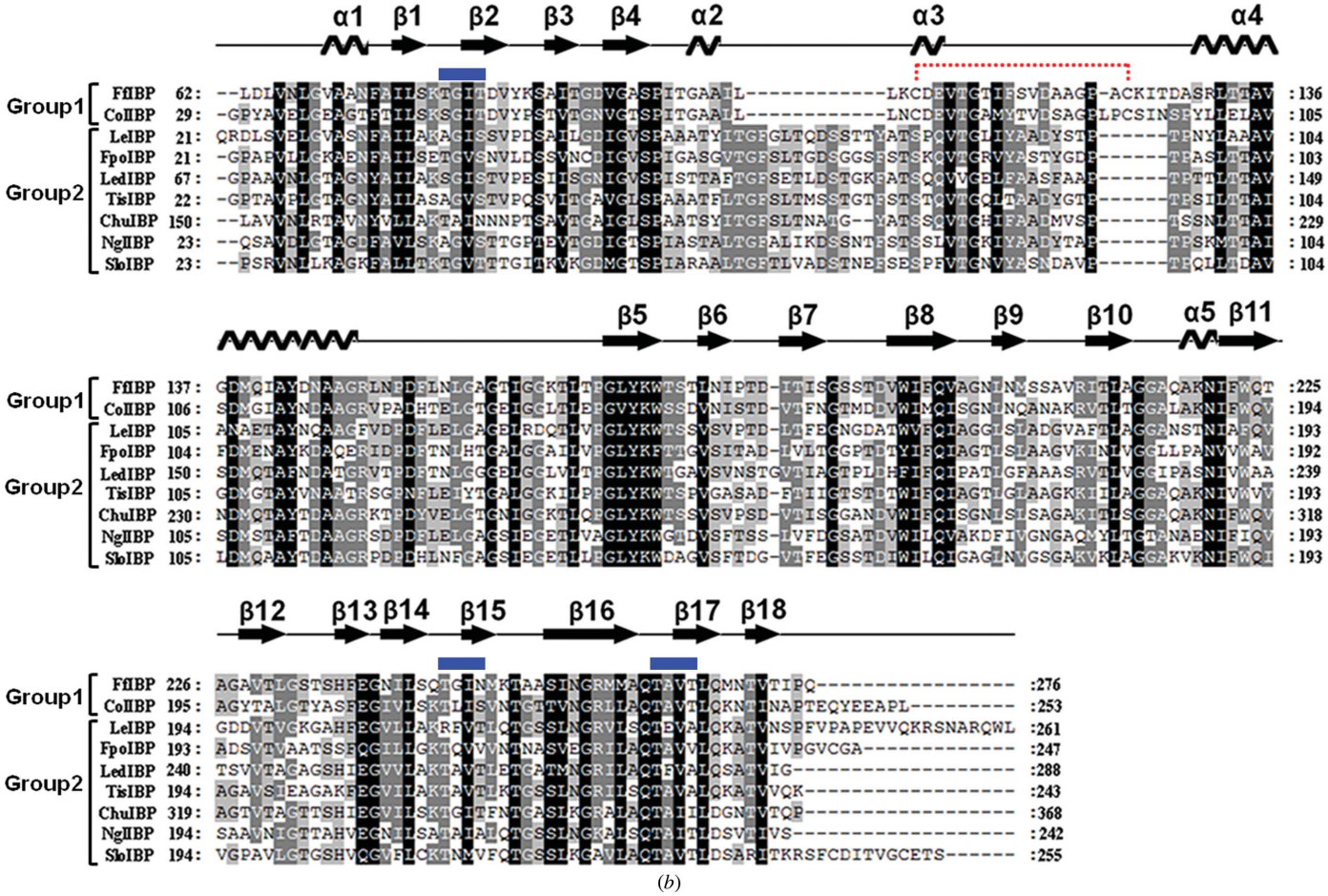

(*b*)

Figure 2
Crystal structure of FfIBP. (*a*) The ribbon diagram of FfIBP adopts a right-handed β-helical fold and is similar to a trigonal prism shape with three parallel sheets (faces *A*, *B* and *C*). The N- and C-termini are labelled. (*b*) Structure-based alignment of the amino-acid sequences of IBPs from *Flavobacterium frigoris* PS1 (FfIBP), *Colwellia* sp. SLW05 (ColIBP), *Leucosporidium* sp. AY30 (LeIBP), *Flammulina populicola* (FpoIBP), *Lentinula edodes* (LedIBP), *Typhula ishikariensis* (TisIBP), *Cytophaga hutchinsonii* ATCC 33406 (ChuIBP), *Navicula glaciei* (NglIBP) and *Stephos longipes* (SloIBP) using *ClustalX* (Thompson *et al.*, 1997). The T-A/G-*X*-T/N motifs constituting the ice-binding sites are indicated by blue bars. Cysteine residues joined by a red dotted line represent disulfide-bond formation.

between 0 and 500 μM. The temperature was raised slowly until a single ice crystal remained. The temperature was lowered again slowly (at approximately 0.5 K min^{-1}) while the ice-crystal morphology was maintained. The freezing point of the sample was determined to be the temperature at which rapid growth of the ice crystal was observed under the microscope. The maximum difference between the annealing temperature and the freezing point during the slow-cooling steps was taken as the TH activity of the sample. The photographs were captured using a Canon PowerShot 620.

2.5. Recrystallization-inhibition assay

All FfIBP samples were dissolved in distilled water and an equal volume of a 60% sucrose solution was mixed with the FfIBP solution. 4 µl of the mixed sample solution was sandwiched between two round 16 mm diameter cover slips. The sandwich droplet was pre-chilled to prevent frost on the surface at 4°C. After 1 min, the sandwich droplet was cooled to −70°C at a rate of 90°C min^{-1} on a circulating cooling stage (THMS600 stage, Linkam Scientific Instruments, Tadworth, England) and then incubated for 60 min at −6°C to allow ice recrystallization. The sandwich droplet was examined under a microscope (Olympus BX51) and images were captured using a DP71 CCD camera (Olympus) every 10 min.

2.6. Docking model of the ice–IBP interaction

Molecular docking of IBPs to the basal plane of the ice crystalwas carried out using the *Hex* program (Ritchie & Kemp, 2000) to obtain better insight into the molecular details of the interaction. A Windows version of the *Hex* software for rigid-body docking (Ritchie & Kemp, 2000) was used to simulate the ice–IBP interaction. Both shape and electrostatics correlation algorithms were used with a search radius of n = 30, and the top docking solution was inspected and presented using the *PyMOL* program (DeLano, 2002).

2.7. Circular-dichroism (CD) spectroscopy

Thermal denaturation of IBPs was monitored using CD spectroscopy on a Chirascan CD spectropolarimeter (Applied Photophysics, Surrey, England) connected to a Peltier temperature controller. Protein samples (20 μM) in 10 mM Tris–HCl pH 8.0, 150 mM NaCl and a 1 mm path-length cuvette were used for spectral data collection. Changes in ellipticity (θ) were recorded at a wavelength of 222 nm by heating the protein sample between 10 and 90°C and ramping the temperature by 1°C. The scan was performed two times at every point and averaged. Melting temperatures (T_m) were decided as the point at which 50% of the sample denatured.

2.8. Equilibrium sedimentation

Equilibrium sedimentation studies were performed at 20°C in 20 mM Tris–HCl buffer pH 8.5 containing 150 mM NaCl and 1 mM DTT using a Beckman ProteomeLab XL-A analytical ultracentrifuge. FfIBP samples were measured at 280 nm using a six-sector cell at rotor speeds of 20 000 and 24 000 rev min^{-1}. All measured data fitted well to a homogeneous monomer (1×) model, and a representative result measured at 24 000 rev min^{-1} using a protein concentration of 11.1 μM is presented. The concentration of the FfIBP protein was calculated using $\varepsilon_{280\,nm}$ = 22 460 M^{-1} cm^{-1} and a molecular weight of 25 715 Da and included two additional amino acids (histidine–methionine) from the cloning process. The time required to attain equilibrium was established by running the experiment at the given rotor speeds until the scans were invariant for 4 h: this was achieved after at most 60 h in the six-sector cells. The partial specific volume of the protein and buffer density were calculated using *Sednterp* (Hayes *et al.*, 1995). The calculated partial specific volume at 20°C was 0.7338 cm^3 g^{-1} and the buffer density was 1.00496 g cm^{-3}. For data analysis by mathematical modelling using nonlinear least-squares curve fitting, the following fitting function was used for the homogeneous model:

$$C_r = C_b \exp[A_p M_p (r^2 - r_b^2)] + \varepsilon,$$
$$A_p = (1 - v\rho)\omega^2 / 2RT, \quad (1)$$

where C_r is the total concentration at the radial position r, C_b is the concentration of protein at the cell bottom, M_p is the molecular weight of the protein, v is the partial specific volume, ρ is the solution density, ω is the rotor angular velocity and ε is a baseline-error term. The model was selected by examining the weighted sum or square values and the weighted root-mean-square error values. Further data manipulation and data analysis by mathematical modelling were performed using *MLAB* (Knott, 1979) operating on the data-analysis computer.

3. Results

3.1. Overall structure of FfIBP

The structure of FfIBP (residues 29–276; the first 28 residues, which were predicted to form a signal sequence, were removed) was determined to a resolution of 2.1 Å using molecular replacement (Petersen *et al.*, 2011) with the monomer structure of LeIBP (Lee *et al.*, 2012) as a model. The overall structure of FfIBP is a β-helical fold consisting of a large coiled structural domain and a long helical α4 insertion between α3 and β5 formed by residues 130–148. The β-helical folds are stabilized by both intramolecular β-sheet hydrogen bonds and inner hydrophobic interactions. Overall, the β-helical core structure is constructed from three flat faces (faces *A*, *B* and *C*) with dimensions of ∼50 × 30 × 20 Å (Fig. 2*a*). These faces are derived from β-strands 1, 4, 5, 8, 11, 14 and 16 (face *A*); 2, 6, 9, 12, 15 and 17 (face *B*); and 3, 7, 10, 13, 16 and 18 (face *C*; Fig. 2). Helices α1, α2, α3 and α5 form a short turn of 3_{10}-helices and the long helix α4 packs against the *A* face of the core β-helical structure of FfIBP, which is quite similar to that observed in the LeIBP structure (Lee *et al.*, 2012). Unlike the LeIBP structure, the FfIBP structure contains an intramolecular disulfide bond, which is located in the loop region (residues 103–129) between α2 and α4. A high electron density was observed between Cys107 and Cys124 during the structure-refinement process, indicating the

presence of a disulfide bond, and the $C^{\beta}-C^{\beta}$ distance between Cys107 and Cys124 was 3.9 Å (Figs. 2*a* and 3*a*). Sequence comparison between FfIBP and LeIBP shows that the major differences are in the head loop region connecting α2–α4, where the disulfide bond is located. Taken together, structural and sequence comparison revealed that the Cys-containing loop region is quite different from those of other IBPs, including LeIBP and TisIBP (Lee *et al.*, 2012; Kondo *et al.*, 2012). Based on the multiple sequence-alignment results, we propose here that IBPs can be classified into two groups, where group 1 is the disulfide bond-containing group, including FfIBP, and group 2 does not possess a disulfide bond, as in LeIBP (Fig. 2*b*). Furthermore, the circular-dichroism (CD) thermal profile showed that disulfide bond-containing FfIBP is more stable than cysteine-containing FfIBP (Fig. 4*c*). We conclude that the change in denaturation temperature is owing to breakage of the intramolecular disulfide bond in the presence of dithiothreitol (DTT). Thus, the intramolecular disulfide bond is important for the structural stability of FfIBP and a substantial decrease in TH activity was observed after the addition of DTT, probably owing to decreased protein stability (Fig. 4*a*).

Based on the structural comparison between FfIBP and LeIBP, the largest structural variability is found in the loop region between α2 and α4 and in the C-terminal region. Notably, the C-terminal residues (243-PFVPAPEVV-251) have been identified as being important for dimerization in LeIBP (Lee *et al.*, 2012; Park *et al.*, 2012). However, the extended C-terminal loop region is not seen in FfIBP and TisIBP (Kondo *et al.*, 2012; Fig. 3*b*). Therefore, we expected that FfIBP might be a monomer in solution. Notably, most of the residues constituting the β4 strand, α4 helix, β5 strand, β8 strand and β16 strand are highly conserved in all group 1 and group 2 IBPs. We have found that these highly conserved residues play an important role in stabilization of the FfIBP structure. For example, the six amino acids (residues 169-PGLYKW-174) of the β5 strand constituted the most highly conserved motif of the protein, and it has been proposed that this region is involved in stabilization of the α4–β5 connecting loop (Lee *et al.*, 2012). Moreover, the highly conserved Trp194 residue on β8 also contributes to the stabilization of the α4–β5 connecting loop by hydrophobic interactions with Ile186, Ile221 and Pro169. The Tyr143 residue on α4 forms a hydrogen bond to Gln224, which may stabilize the conformation of helix α4. On the other hand, the ice-binding residues are relatively divergent (30–40% sequence identity) among IBPs, suggesting that the sequence variation may confer distinct antifreeze activities upon IBPs.

3.2. FfIBP is a monomer in solution

The recombinantly produced FfIBP was crystallized in space group $P4_122$ containing one monomer in the asymmetric unit. The results of size-exclusion chromatography (SEC; Figs. 5*a* and 5*b*) and analytical ultracentrifugation (AUC) showed that FfIBP was present mainly in the monomeric state (Harding & Horton, 1992; Fig. 5*c*). Fig. 5(*c*) shows data from equilibrium sedimentation measurements and fits for an FfIBP monomer (1×) and dimer (2×) at an ultracentrifugal speed of 24 000 rev min^{-1}. The weighted root-mean-square (r.m.s.) error values for the 1× and 2× fits were 7.36×10^{-3} and 2.97×10^{-2}, respectively, indicating the superiority of the monomer model. In the inset in Fig. 5, residual plots are also shown. Whereas the monomer model (filled circle) shows a random residual distribution, the dimer model (square) shows systematic deviations throughout the radial positions. Equilibrium sedimentation data measured at 20 000 rev min^{-1} also support the reversible 1× model (data not shown).

3.3. Antifreeze activity of FfIBP

The temperature gap between the melting points and freezing points of solutions of purified FfIBP were assayed and used to produce a standard curve of TH activity. The FfIBP exhibited TH activities of 2.2°C at 5 µ*M* and 2.5°C at 50 µ*M*. The TH activity of FfIBP is tenfold higher than that of LeIBP at equivalent concentrations, and indeed it is the only

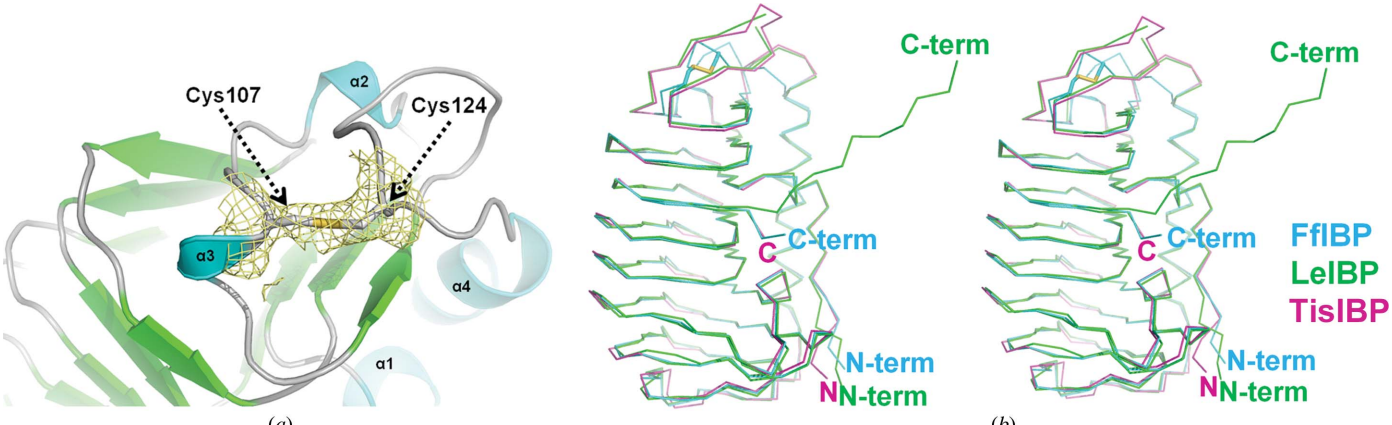

Figure 3
Intramolecular disulfide-bond formation in FfIBP. (*a*) The $2F_o - F_c$ electron-density map (contoured at 1σ) around the Cys107–Cys124 bond is shown. (*b*) Structural comparison of FfIBP (cyan), LeIBP (green) and TisIBP (magenta). Superimposition of FfIBP onto other known IBP structures revealed that FfIBP adopts a novel conformation of the capping head loop region containing an intramolecular disulfide bond formed between the Cys107 and Cys124 residues. The N- and C-termini are labelled and disulfide bonds are shown as yellow sticks.

known IBP with a specific activity comparable with those of insect AFPs (Do *et al.*, 2012). As seen in insect AFPs, the morphology of the ice crystals resembled a hexagonal or lemon shape (Fig. 6*a*). When the TH gap is exceeded, the crystals burst in the plane of the *a* axes. This behaviour indicates that FfIBP is clearly hyperactive and that it may protect the basal planes as well as the prism planes {1 0 −1 0} or {1 1 −2 0} from ice growth, which is consistent with the dual-plane ice-binding mode of hyperactive AFPs (Venketesh & Dayananda, 2008; Jia & Davies, 2002; Graether *et al.*, 2000).

In addition, the recrystallization inhibition (RI) activity of FfIBP was measured and is shown in Fig. 6(*b*). FfIBP effectively inhibited the recrystallization of ice, while the negative control, BSA solution, did not. RI activity assays were performed at three different concentrations of FfIBP. Even at a concentration of 1.05 μ*M*, FfIBP showed clear RI activity; therefore, FfIBP has strong RI activity as well as high TH activity (Fig. 6*b*). Furthermore, we performed site-directed mutagenesis to investigate the structure–function relationships and to identify the ice-binding residues of FfIBP. A tyrosine residue was introduced at the mutation site, which confers steric hindrance to ice binding and causes a large reduction in antifreeze activity at the ice-binding face (Lee *et al.*, 2012). The N248Y, T251Y and T266Y mutations on the *B* face significantly reduced the TH activity of FfIBP (to 43, 11 and 33% of the activity of the wild-type protein, respectively; 60 μ*M* protein concentration). In contrast, residues on the *C* face (Thr211 and Thr234) do not affect the TH activity, indicating that the ice-binding site of FfIBP is on the *B* face and that the Asn248, Thr251 and Thr266 residues are involved in ice binding (Fig. 6*c*).

3.4. Ice-binding site of FfIBP

Based on the structural comparison of FfIBP and LeIBP, we found that the difference in antifreeze activity may be

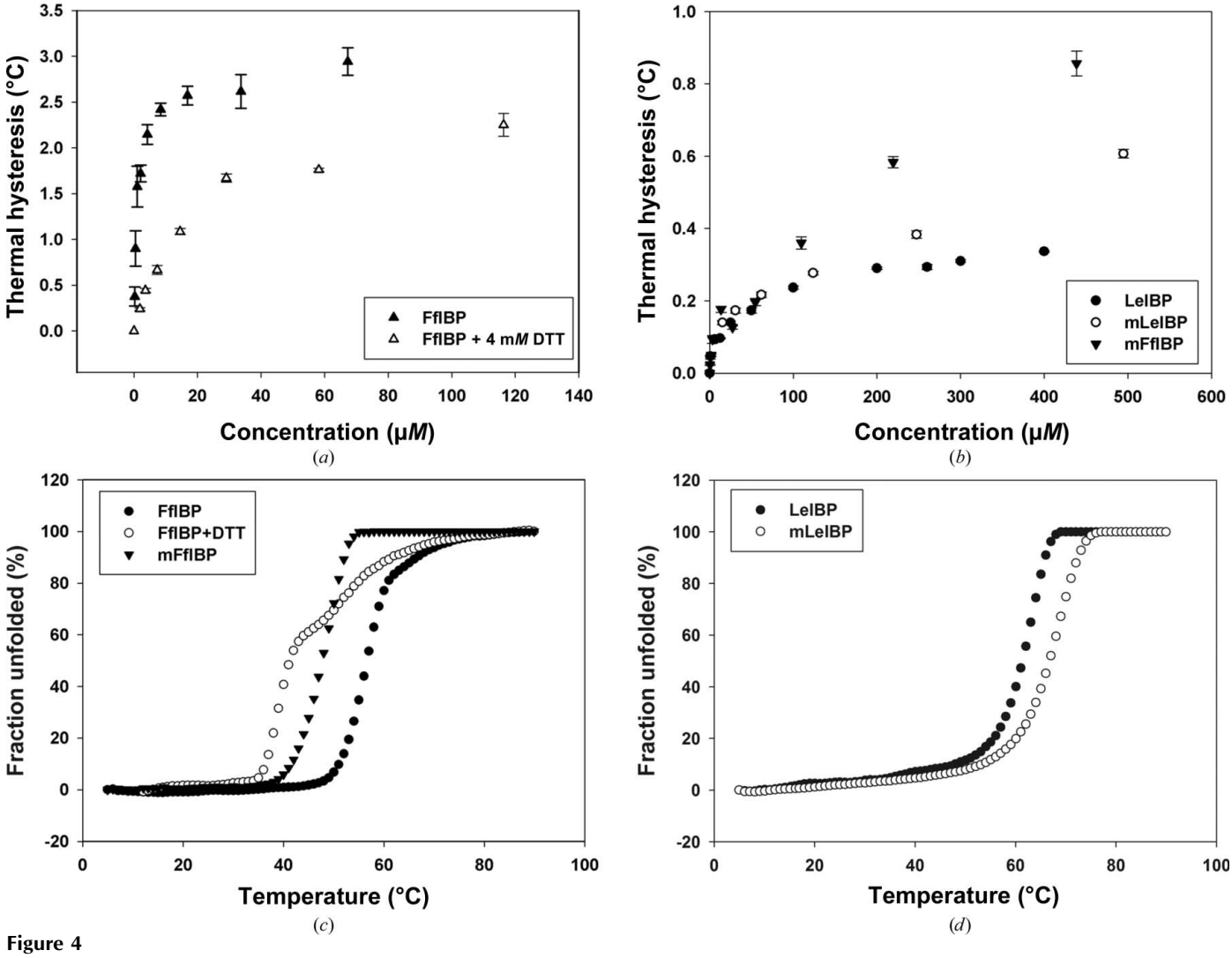

Figure 4
TH activity and thermal stability of IBPs. (*a*) TH activity curve of FfIBP in the absence and presence of 4 m*M* DTT. (*b*) TH activity of LeIBP, mLeIBP and mFfIBP. Each point was measured three times and averaged. (*c*) CD spectra demonstrating the thermal denaturation of FfIBP (filled circles), FfIBP with 4 m*M* DTT (open circle) and mFfIBP (filled triangle). (*d*) CD spectra demonstrating the thermal denaturation of LeIBP (filled circles) and mLeIBP (open circles).

attributable to the amino-acid composition in the ice-binding site. Despite their high sequence (39% sequence identity and 56% sequence homology) and structural (r.m.s.d. of 2.0 Å for all C^{α} atoms) similarities, the LeIBP and FfIBP structures showed large differences in ice-binding site residues. When the structures were compared, it was clearly seen that FfIBP has an aligned ice-binding motif (T-A/G-*X*-T/N). In this regard, the ice-binding residues of FfIBP are similar to those of the hyperactive insect AFPs. The distance between two ice-binding residues along a strand is approximately 10.1 Å, which is close to the spacing of O atoms on the basal plane of ice (10.3 Å). The spacing between Thr residues on adjacent strands is close to 4.5 Å, similar to those of insect AFPs. Therefore, the ice-binding motif of FfIBP is well matched to the geometric lattice of water molecules in ice (Figs. 7*a* and 7*c*). Moreover, there are additional ice-binding residues such as Thr or Asn on the *B* face of the FfIBP structure besides the ice-binding motif (T-A/G-*X*-T/N). We suspect that these residues also contribute to the induction of ice binding of FfIBP at additional sites after initial ice binding between ice-binding motifs and ice crystals. Notably, the total number of Thr or Asn residues involved in ice binding for FfIBP (13 residues) is greater than that of LeIBP (four residues; Figs. 7*a* and 7*b*).

To investigate the ice-binding properties of FfIBP and LeIBP, binding models were constructed using the *Hex* program (Ritchie & Kemp, 2000) and the *B* face of IBPs docked onto a basal plane surface of an ice crystal (Fig. 8). Tight contacts between the IBPs and the basal plane of the ice crystal result in extensive interactions, with a buried surface area of ~620 Å^2 in FfIBP and ~410 Å^2 in LeIBP. It is clear that the specific TH activity increases with the surface area of the ice-binding site of AFP. This is a generally accepted concept in AFPs. For example, a natural isoform of the spruce budworm AFP with eight β-helical loops is three times more active than the abundant isoform containing six β-helical loops, and an engineered variant of the *Tenebrio molitor* AFP with two added coils is twice as active as the wild-type AFP (Leinala *et al.*, 2002; Marshall *et al.*, 2004). The larger isoform (15.7 kDa) AFP from the snow flea also exhibits a severalfold higher TH activity than the smaller isoform (6.5 kDa) (Mok *et al.*, 2010). Moreover, simple fusions of AFPs to generate tandem AFP repeats also enhanced TH activity through an increase in ice-binding site area (Liou *et al.*, 2000). Taken together, our structural studies indicate that the aligned ice-binding motif residues and greater ice-binding area may confer hyper-antifreeze activity on FfIBP. Notably, 15 ordered water molecules are observed at this surface in the FfIBP crystal structure and their potential displacement would create a significant favourable binding surface for the ice crystal.

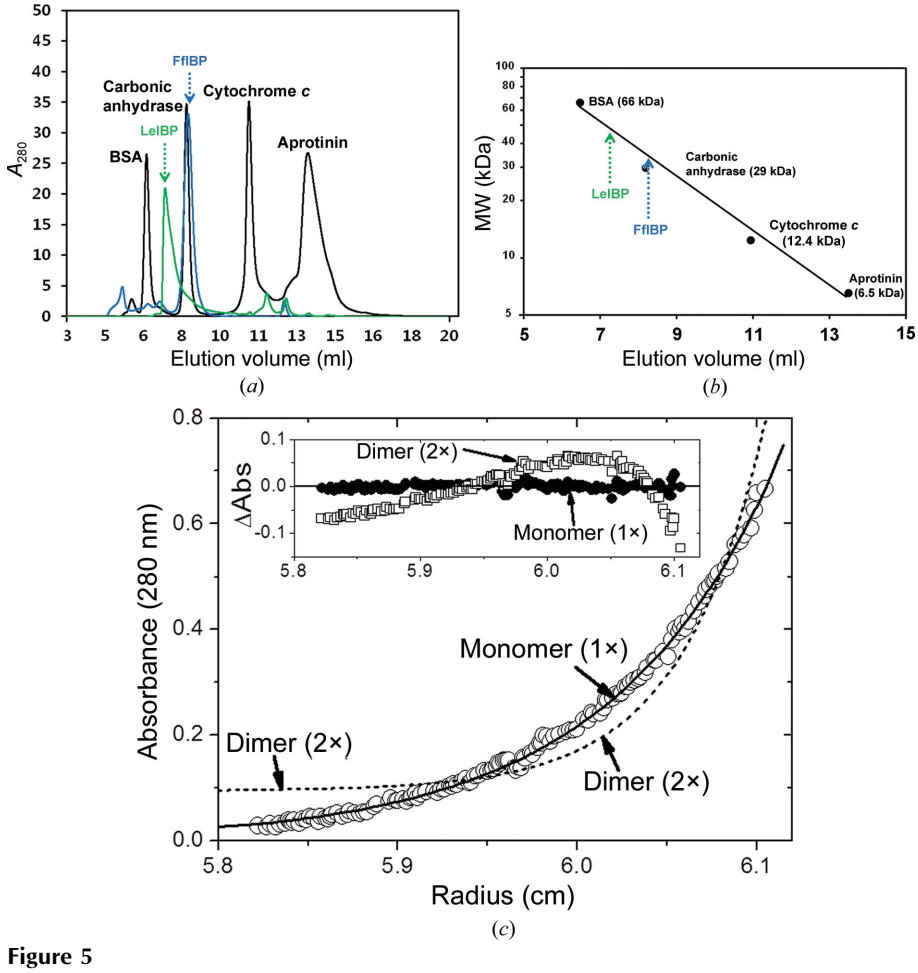

Figure 5
Molecular weight and oligomeric state of FfIBP. (*a*, *b*) Size-exclusion chromatography of FfIBP, LeIBP (dimer) and size-marker proteins using a TSK G2000SWxl column equilibrated with ten column volumes of 20 m*M* Tris–HCl pH 8.0, 150 m*M* NaCl at a flow rate of 1 ml min^{-1} at 22°C. The black line represents the elution volume of the standard proteins used for calibration. The protein standards were bovine serum albumin (66 kDa), carbonic anhydrase (29 kDa), cytochrome *c* (12.4 kDa) and aprotinin (6.5 kDa). (*c*) The molecular weight of FfIBP was independently confirmed by analytical ultracentrifugation (AUC) and the sedimentation-equilibrium distribution (circle) of the FfIBP protein is shown. The concentration of the protein was 11.1 µ*M* (0.29 mg ml^{-1}). The circles are the experimental data at 280 nm and the solid line is the fit for a homogeneous monomer (1×) model. The dotted line is the fit for a homogeneous dimer (2×) model. The calculated molecular mass for an FfIBP monomer based on its amino-acid composition is 25 715 Da. Inset, distributions of the residuals for monomer (1×, filled circle) and dimer (2×, square). The random distributions of the residuals for the 1× model indicate that FfIBP exists as homogeneous monomers in solution. The homogeneous 2× model shows systematic deviations.

3.5. Capping head region of FfIBP

In this study, we have swapped the capping head region and generated two novel chimeric proteins, mFfIBP and mLeIBP (Fig. 1*a*), to address the structural and functional roles of the capping

head region, which is the major difference between LeIBP and FfIBP. Moreover, crystallization trials were carried out with these two chimeric mutants and the crystal structures of mFfIBP and mLeIBP have been determined at 1.4 and 1.34 Å resolution, respectively. The overall protein folds of the two chimeric structures are very similar to that of the corresponding template wild-type IBP except in the capping head region (Figs. 1*b* and 1*c*). Interestingly, however, the TH activity of mFfIBP was significantly reduced compared with that of wild-type FfIBP (greater than sevenfold). We assumed that the low activity might be related to the thermal instability of the chimeric protein. In our thermal denaturation experiments, mFfIBP (T_m value of 47.4°C) had a significantly lower thermal denaturation temperature compared with FfIBP (T_m value of 56.4°C). Conversely, chimeric mLeIBP (T_m value of 66.4°C) with the capping head region of FfIBP had a slightly increased TH activity compared with LeIBP (T_m value of 61°C). The T_m value of mLeIBP was also greater than that of LeIBP (Fig. 4). Thus, it is clear that the capping head region of FfIBP is more stable than that of LeIBP and is important for the overall stability of IBP, although it is not directly involved in antifreeze activity. This may be because of the short length and rigidity of the capping head loop region of FfIBP owing to the presence of the covalent disulfide-bond linkage. In fact, it is generally accepted that an increase in loop length and flexibility usually results in a decrease in protein stability.

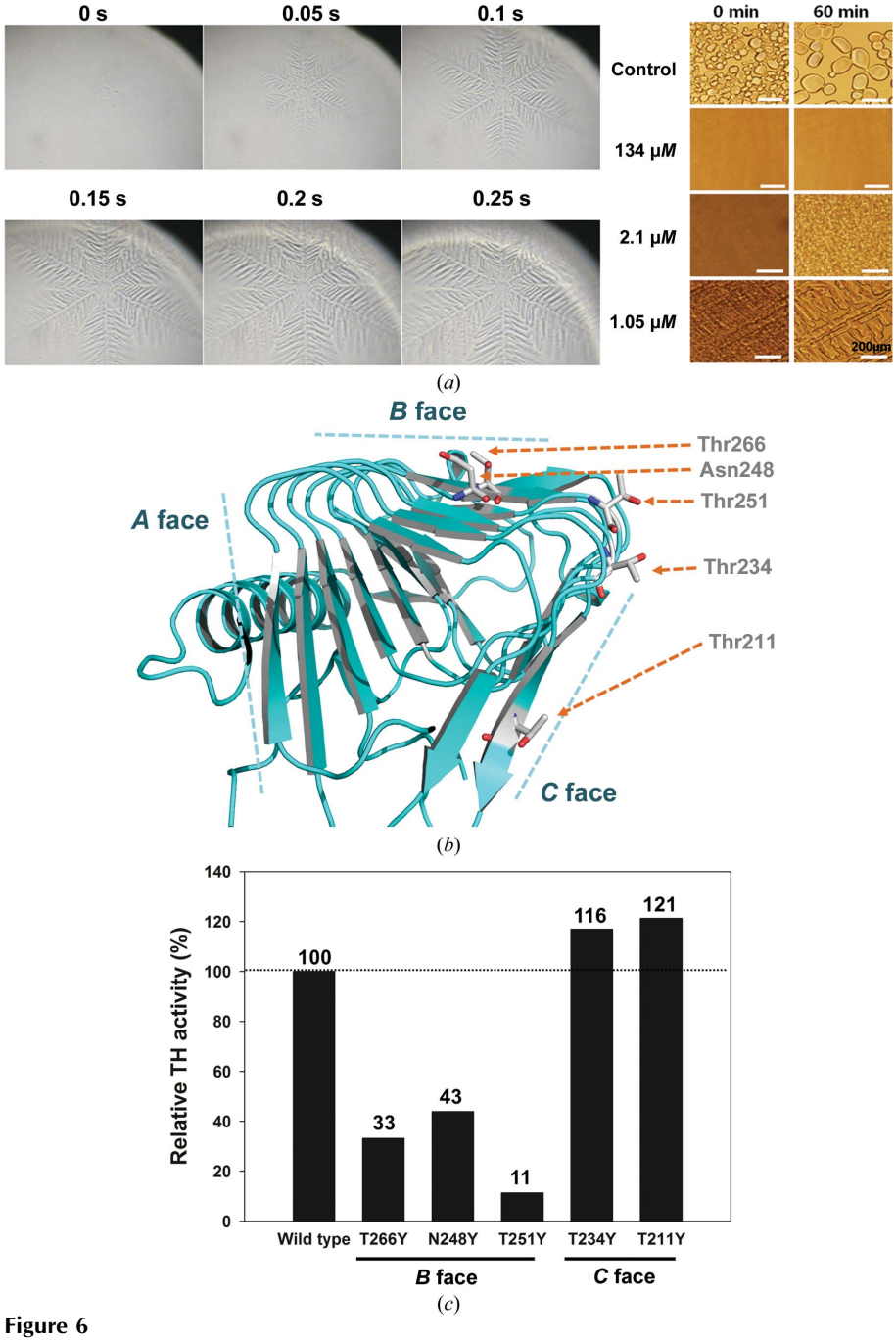

Figure 6
Antifreeze properties and ice-binding site of FfIBP. (*a*) Ice crystals were grown in solutions of 4.2 µ*M* FfIBP. Burst ice-crystal morphology was shown after the temperature dropped below the TH gap in the presence of recombinant FfIBP. (*b*) Inhibition of ice recrystallization by FfIBP. The first row shows RI assays using BSA protein (30 µ*M*) as the negative control. The remaining rows show the RI activities of FfIBP at three different concentrations (134, 2.1 and 1.05 µ*M*). (*c*) TH activity comparison of wild-type FfIBP and the mutants at 60 µ*M* concentration. The location of each mutation in the FfIBP structure is labelled and shown as a stick model.

4. Discussion

Type I, type II and type III plant and insect AFPs are representative examples of convergent evolution because they are entirely different proteins but perform the same function. New IBPs have been identified and characterized from various organisms such as yeast, diatoms, fungi, algae and bacteria, but they share a similar sequence, tertiary structure and common function: adsorbing to ice. Recent studies suggest that horizontal transfer of the IBP gene from bacteria to other organisms occurred in order to acquire the cold-adaptation mechanism. Horizontal gene transfer between different organisms is thought to occur rarely, but these transfers may occur more frequently if they share the same habitat such as the extremely cold polar region (Raymond *et al.*, 2007; Raymond & Kim, 2012). However, although IBPs exhibit similar architectures, their ice-binding residues differ significantly. As secreted proteins, IBPs are also subject to at least some post-translational modification, such as signal peptide cleavage, glycosylation and disulfide-bond formation.

We have screened polar organisms which express IBPs. We previously identified and characterized a glycosylated IBP, LeIBP, from an Arctic yeast. In this study, we extended this work by examining the structure of FfIBP from the Antarctic bacterium *F. frigoris* PS1, revealing the architecture of the ice-binding motif and the presence of an intramolecular disulfide bond. The FfIBP structure determined here is the first of an IBP showing an intramolecular disulfide bridge, which allows us to classify the IBPs into two subgroups. Despite the species diversity among members of the IBP family, analysis of the LeIBP and FfIBP structures suggests that IBPs have a common structural domain required for ice binding and adopt right-handed β-helical structures. However, FfIBP shows a different antifreeze activity and oligomerization state compared with LeIBP. Unlike LeIBP, FfIBP is a monomer in solution and has a shorter C-terminal loop region. Notably, the cleavage of the C-terminal loop region resulted in a 13% increase in TH activity in LeIBP, because these residues make direct contacts for dimerization and the C-terminally truncated LeIBP was monomeric in solution (Lee *et al.*, 2012; Park *et al.*, 2012). Multiple sequence alignment (Fig. 2*b*) suggests that the C-terminal loop region is the most variable region in IBPs. These extra C-terminal residues are not well conserved in other IBP sequences, suggesting that dimer formation is a unique feature of LeIBP. Therefore, we had predicted that preventing dimerization might cause LeIBP to be more freely accessible for ice binding in the monomeric state, which may confer higher TH activity to the C-terminally truncated LeIBP

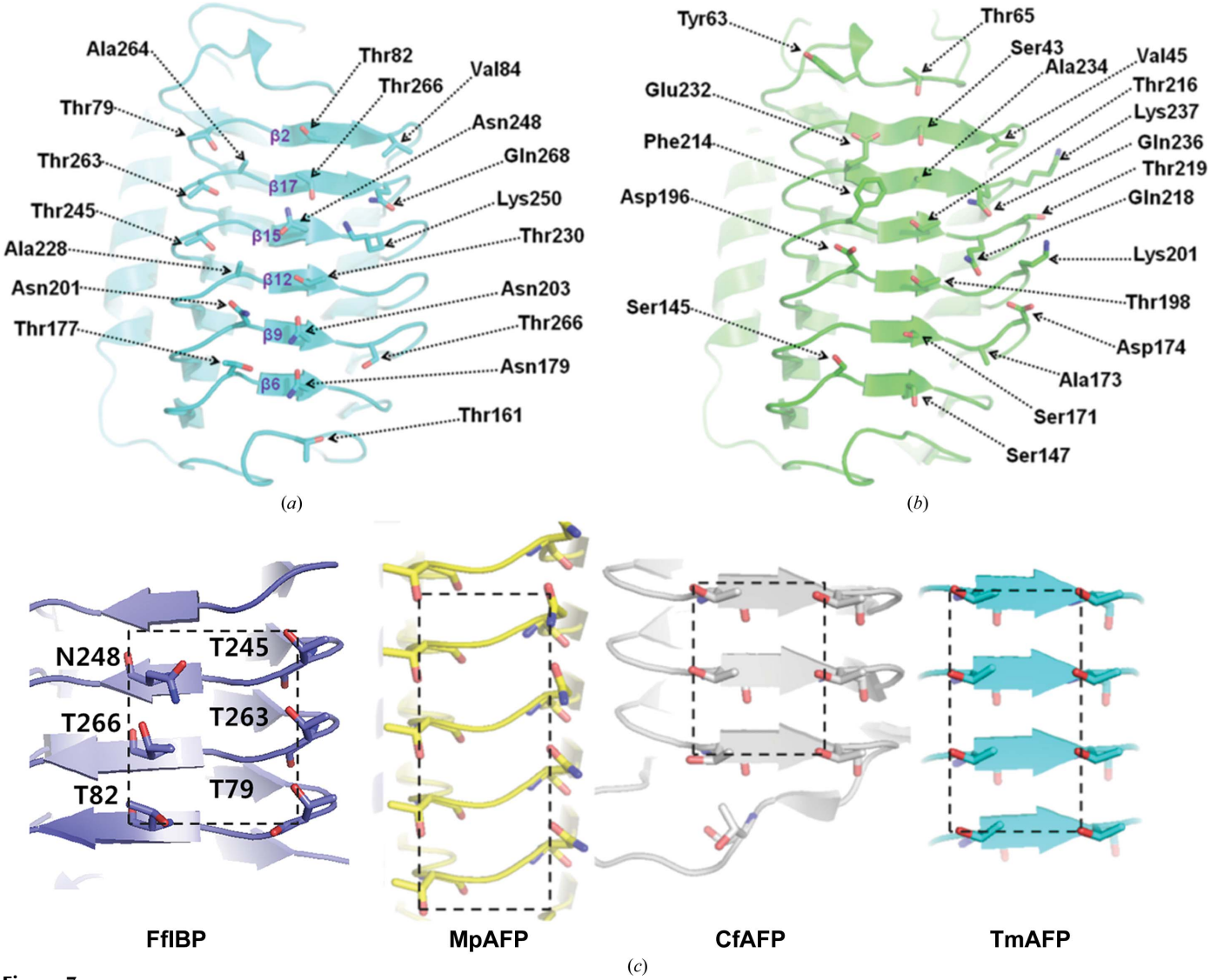

Figure 7
Comparison of ice-binding sites of FfIBP with other β-helical fold IBPs. (*a*) Ice-binding residues on the *B* face of FfIBP. The ice-binding site of FfIBP has a very high Thr and Asn residue content. (*b*) Ice-binding residues on the *B* face of LeIBP. The ice-binding site residues of LeIBP are more diverse compared with the FfIBP structure. (*c*) The ice-binding site of FfIBP contains an ice-binding motif (T-A/G-*X*-T/N), while MpAFP (from *Marinomonas primoryensis*) has a T-*X*-N motif and CfAFP (from *Choristoneura fumiferana*) and TmAFP (from *Tenebrio molitor*) use a T-*X*-T motif for ice binding. Only the first and last residues of the ice-binding motif are connected in rectangular boxes to compare the ice-binding areas with one another. Notably, FfIBP contains three ice-binding motifs (T-A/G-*X*-T/N) on the *B* face, while LeIBP does not have a recognizable ice-binding motif. O and N atoms are shown in red and blue, respectively.

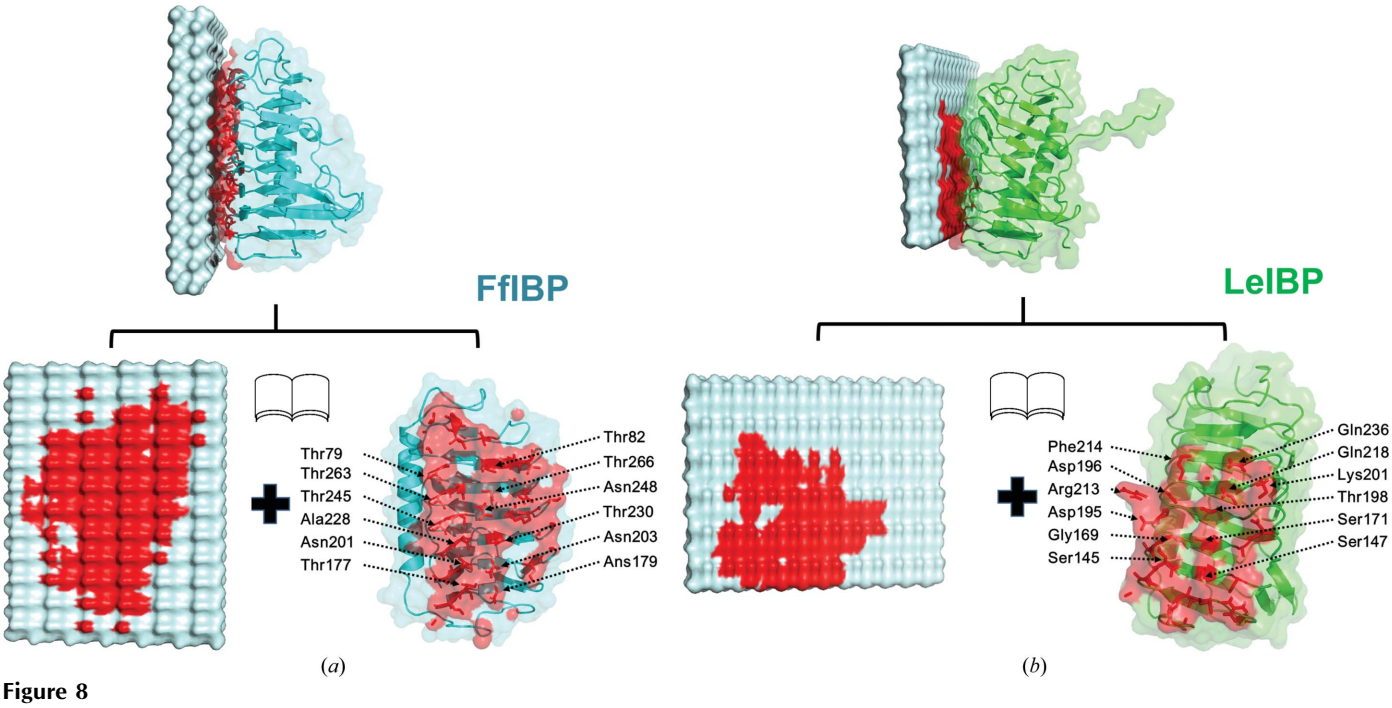

Figure 8
Comparison of the ice-binding interface areas of FfIBP and LeIBP. (*a*) Open-book view of the ice-binding interface of FfIBP. The solvent-accessible molecular surface of FfIBP is shown semi-transparently over a representation of the secondary structure to illustrate the complementarity of the binding surfaces. Each interface is coloured red and the ice-binding residues of FfIBP are shown as red stick representations. (*b*) Open-book view of the ice-binding interface of LeIBP. Each interface is coloured red and the ice-binding residues of LeIBP are indicated as red sticks. The ice-binding interface of FfIBP has a larger surface area (∼620 Å^2) than that of LeIBP (∼410 Å^2), with good shape complementarity. The residues involved in ice binding are indicated as red sticks.

mutant. Hence, we suggest here that the absence of the C-terminal region clearly renders FfIBP more active to ice binding, and this might be one of the reasons for the difference in antifreeze activity between FfIBP and LeIBP. The hyperactivity of FfIBP also can be explained in terms of the residue composition of the ice-binding site. The ice-binding site of FfIBP is much flatter and it has more regular ice-binding motif residues than LeIBP. Conclusively, our results provide a molecular basis for understanding the reasons for the hyperantifreeze activity of FfIBP. New IBPs have been identified from various organisms; thus, there is clearly still much to be learned from studying the structural biology of IBPs.

We thank the staff at the 5C and 7A beamlines of Pohang Accelerator Laboratory (PAL; Pohang, Republic of Korea) for their kind help with data collection. Preliminary X-ray diffraction analyses were performed at the X-ray facility home source of Korea Basic Science Institute (KBSI; Ochang, Republic of Korea). This work was supported by the Korea Polar Research Institute (KOPRI; grant No. PE14070).

References

Achenbach, J. C. & Ewart, K. V. (2002). *Eur. J. Biochem.* **269**, 1219–1226.
Adams, P. D. *et al.* (2010). *Acta Cryst.* D**66**, 213–221.
Antson, A. A., Smith, D. J., Roper, D. I., Lewis, S., Caves, L. S., Verma, C. S., Buckley, S. L., Lillford, P. J. & Hubbard, R. E. (2001). *J. Mol. Biol.* **305**, 875–889.
Bayer-Giraldi, M., Weikusat, I., Besir, H. & Dieckmann, G. (2011). *Cryobiology*, **63**, 210–219.
Chen, V. B., Arendall, W. B., Headd, J. J., Keedy, D. A., Immormino, R. M., Kapral, G. J., Murray, L. W., Richardson, J. S. & Richardson, D. C. (2010). *Acta Cryst.* D**66**, 12–21.
D'Amico, S., Collins, T., Marx, J. C., Feller, G. & Gerday, C. (2006). *EMBO Rep.* **7**, 385–389.
Davies, P. L., Baardsnes, J., Kuiper, M. J. & Walker, V. K. (2002). *Philos. Trans. R. Soc. Lond. B Biol. Sci.* **357**, 927–935.
DeLano, W. L. (2002). *PyMOL*. http://www.pymol.org.
Do, H., Lee, J. H., Lee, S. G. & Kim, H. J. (2012). *Acta Cryst.* F**68**, 806–809.
Doucet, D., Tyshenko, M. G., Kuiper, M. J., Graether, S. P., Sykes, B. D., Daugulis, A. J., Davies, P. L. & Walker, V. K. (2000). *Eur. J. Biochem.* **267**, 6082–6088.
Drenth, J. (1999). *Principles of Protein X-ray Crystallography*, pp. 219–243. New York: Springer.
Emsley, P., Lohkamp, B., Scott, W. G. & Cowtan, K. (2010). *Acta Cryst.* D**66**, 486–501.
Garnham, C. P., Campbell, R. L. & Davies, P. L. (2011). *Proc. Natl Acad. Sci. USA*, **108**, 7363–7367.
Garnham, C. P., Gilbert, J. A., Hartman, C. P., Campbell, R. L., Laybourn-Parry, J. & Davies, P. L. (2008). *Biochem. J.* **411**, 171–180.
Graether, S. P., Kuiper, M. J., Gagné, S. M., Walker, V. K., Jia, Z., Sykes, B. D. & Davies, P. L. (2000). *Nature (London)*, **406**, 325–328.
Graether, S. P. & Sykes, B. D. (2004). *Eur. J. Biochem.* **271**, 3285–3296.
Hakim, A., Nguyen, J. B., Basu, K., Zhu, D. F., Thakral, D., Davies, P. L., Isaacs, F. J., Modis, Y. & Meng, W. (2013). *J. Biol. Chem.* **288**, 12295–12304.
Harding, S. E. & Horton, J. C. (1992). *Analytical Ultracentrifugation in Biochemistry and Polymer Science*. Cambridge: Royal Society of Chemistry.
Hayes, D., Laue, T. & Philo, J. (1995). *Sednterp*. University of New Hampshire, Durham, New Hampshire, USA. http://bitcwiki.sr.unh.edu.

Hoshino, T., Kiriaki, M., Ohgiya, S., Fujiwara, M., Kondo, H., Nishimiya, Y., Yumoto, I. & Tsuda, S. (2003). *Can. J. Bot.* **81**, 1175–1181.
Janech, M. G., Krell, A., Mock, T., Kang, J.-S. & Raymond, J. A. (2006). *J. Phycol.* **42**, 410–416.
Jia, Z. & Davies, P. L. (2002). *Trends Biochem. Sci.* **27**, 101–106.
Knott, G. D. (1979). *Comput. Programs Biomed.* **10**, 271–280.
Kondo, H., Hanada, Y., Sugimoto, H., Hoshino, T., Garnham, C. P., Davies, P. L. & Tsuda, S. (2012). *Proc. Natl Acad. Sci. USA*, **109**, 9360–9365.
Krell, A., Beszteri, B., Dieckmann, G., Glöckner, G., Valentin, K. & Mock, T. (2008). *Eur. J. Phycol.* **43**, 423–433.
Kwan, A. H.-Y., Fairley, K., Anderberg, P. I., Liew, C. W., Harding, M. M. & Mackay, J. P. (2005). *Biochemistry*, **44**, 1980–1988.
Lee, J. H., Park, A. K., Do, H., Park, K. S., Moh, S. H., Chi, Y. M. & Kim, H. J. (2012). *J. Biol. Chem.* **287**, 11460–11468.
Lee, J. K., Park, K. S., Park, S., Park, H., Song, Y. H., Kang, S.-H. & Kim, H. J. (2010). *Cryobiology*, **60**, 222–228.
Leinala, E. K., Davies, P. L., Doucet, D., Tyshenko, M. G., Walker, V. K. & Jia, Z. (2002). *J. Biol. Chem.* **277**, 33349–33352.
Leinala, E. K., Davies, P. L. & Jia, Z. (2002). *Structure*, **10**, 619–627.
Liou, Y.-C., Tocilj, A., Davies, P. L. & Jia, Z. (2000). *Nature (London)*, **406**, 322–324.
Liu, Y., Li, Z., Lin, Q., Kosinski, J., Seetharaman, J., Bujnicki, J. M., Sivaraman, J. & Hew, C.-L. (2007). *PLoS One*, **2**, e548.
Marshall, C. B., Chakrabartty, A. & Davies, P. L. (2005). *J. Biol. Chem.* **280**, 17920–17929.
Marshall, C. B., Daley, M. E., Sykes, B. D. & Davies, P. L. (2004). *Biochemistry*, **43**, 11637–11646.
McCoy, A. J., Grosse-Kunstleve, R. W., Adams, P. D., Winn, M. D., Storoni, L. C. & Read, R. J. (2007). *J. Appl. Cryst.* **40**, 658–674.
Middleton, A. J., Marshall, C. B., Faucher, F., Bar-Dolev, M., Braslavsky, I., Campbell, R. L., Walker, V. K. & Davies, P. L. (2012). *J. Mol. Biol.* **416**, 713–724.
Mok, Y.-F., Lin, F.-H., Graham, L. A., Celik, Y., Braslavsky, I. & Davies, P. L. (2010). *Biochemistry*, **49**, 2593–2603.
Murshudov, G. N., Skubák, P., Lebedev, A. A., Pannu, N. S., Steiner, R. A., Nicholls, R. A., Winn, M. D., Long, F. & Vagin, A. A. (2011). *Acta Cryst.* D**67**, 355–367.
Otwinowski, Z. & Minor, W. (1997). *Methods Enzymol.* **276**, 307–326.
Park, K. S., Do, H., Lee, J. H., Park, S. I., Kim, E., Kim, S.-J., Kang, S.-H. & Kim, H. J. (2012). *Cryobiology*, **64**, 286–296.
Park, A. K., Park, K. S., Kim, H. J., Park, H., Ahn, I. Y., Chi, Y. M. & Moon, J. H. (2011). *Acta Cryst.* F**67**, 800–802.
Patel, S. N. & Graether, S. P. (2010). *Biochem. Cell Biol.* **88**, 223–229.
Petersen, T. N., Brunak, S., von Heijne, G. & Nielsen, H. (2011). *Nature Methods*, **8**, 785–786.
Raymond, J. A., Christner, B. C. & Schuster, S. C. (2008). *Extremophiles*, **12**, 713–717.
Raymond, J. A., Fritsen, C. & Shen, K. (2007). *FEMS Microbiol. Ecol.* **61**, 214–221.
Raymond, J. A. & Janech, M. G. (2009). *Cryobiology*, **58**, 151–156.
Raymond, J. A., Janech, M. G. & Fritsen, C. H. (2009). *J. Phycol.* **45**, 130–136.
Raymond, J. A. & Kim, H. J. (2012). *PLoS One*, **7**, e35968.
Ritchie, D. W. & Kemp, G. J. (2000). *Proteins*, **39**, 178–194.
Siemer, A. B. & McDermott, A. E. (2008). *J. Am. Chem. Soc.* **130**, 17394–17399.
Smallwood, M., Worrall, D., Byass, L., Elias, L., Ashford, D., Doucet, C. J., Holt, C., Telford, J., Lillford, P. & Bowles, D. J. (1999). *Biochem. J.* **340**, 385–391.
Thompson, J. D., Gibson, T. J., Plewniak, F., Jeanmougin, F. & Higgins, D. G. (1997). *Nucleic Acids Res.* **25**, 4876–4882.
Vagin, A. & Teplyakov, A. (2010). *Acta Cryst.* D**66**, 22–25.
Venketesh, S. & Dayananda, C. (2008). *Crit. Rev. Biotechnol.* **28**, 57–82.
Xiao, N., Suzuki, K., Nishimiya, Y., Kondo, H., Miura, A., Tsuda, S. & Hoshino, T. (2010). *FEBS J.* **277**, 394–403.